Received: 12 May 2022 | Revised: 23 June 2022 | Accepted: 17 July 2022

DOI: 10.1002/sus2.83

RESEARCH ARTICLE

SusMat WILEY

Regulating nitrogen vacancies within graphitic carbon nitride to boost photocatalytic hydrogen peroxide production

Yanlin Zhu[1] | **Xuetao Liu**[1] | **Heng Liu**[1] | **Guangling He**[1] | **Jiamin Xiao**[1] | **Haijiao Xie**[3] | **Yanyan Sun**[2] | **Lei Han**[1]

[1]College of Materials Science and Engineering, Hunan Joint International Laboratory of Advanced Materials and Technology for Clean Energy, Hunan University, Changsha, Hunan, China

[2]School of Materials Science and Engineering, Central South University, Changsha, Hunan, China

[3]Hangzhou Yanqu Information Technology Co. Ltd., Hangzhou, China

Correspondence
Yanyan Sun, School of Materials Science and Engineering, Central South University, Changsha 410083, Hunan, China.
Email: yanyan.sun@csu.edu.cn

Lei Han, College of Materials Science and Engineering, Hunan Joint International Laboratory of Advanced Materials and Technology for Clean Energy, Hunan University, Changsha 410082, Hunan, China.
Email: hanlei@hnu.edu.cn

Funding information
Huxiang High-Level Talent Gathering Project of Hunan Province, Grant/Award Number: 2019RS1012; Natural Science Foundation of Changsha, Grant/Award Number: KQ2202146; Fundamental Research Funds for the Central Universities, Grant/Award Numbers: 531118010232, 202044011

Abstract

Introducing nitrogen vacancies is an effective method to improve the catalytic performance of g-C_3N_4-based photocatalysts, whereas understanding how nitrogen vacancies types affect the catalytic performance remains unclear. Herein, two different types of nitrogen vacancies were successfully introduced into g-C_3N_4 by pyrolysis of melamine under argon and ammonia atmosphere with subsequent HNO_3 oxidation. The pyrolysis atmosphere is found to have a significant influence on the introduced nitrogen vacancies type, where tertiary nitrogen groups (N_3C) and sp^2-hybridized nitrogen atoms (N_2C) were the preferred sites for the formation of nitrogen vacancies under ammonia and argon pyrolysis, respectively. Moreover, nitrogen vacancies from N_3C are experimentally and theoretically demonstrated to facilitate the narrowed band gap and the improved oxygen absorption capability. As expected, the optimal catalyst exhibits high H_2O_2 yield of 451.8 μM, which is 3.8 times higher than the pristine g-C_3N_4 (119.0 μM) after 4 h and good stability after10 photocatalytic runs.

KEYWORDS
carbon nitride, hydrogen peroxide, nitrogen vacancies, oxygen absorption

1 | INTRODUCTION

Increasing global energy demands with the related environmental issues is promoting the researchers to develop sustainable methods for the production of high-value-added chemicals, such as hydrogen peroxide (H_2O_2).[1–3] In this direction, solar-driven direct production of H_2O_2 from water and molecular oxygen using photocatalysts has recently received growing attention as promising alternative to the conventional industrial 2-alkylanthraquinone process with the use of organic solvent and high energy consumption, since it needs only water, oxygen, and solar energy without carbon emission.[2] Moreover, H_2O_2 as green oxidant and energy carrier has been widely used in many important applications in the fields of chemical industry, environmental remediation, and fuel cell for electricity generation. In order to efficiently utilize solar energy for H_2O_2 production, the key challenge lies in exploring highly efficient and cost-effective photocatalysts operated at moderate reaction conditions.

Currently, many semiconductor materials, such as metal oxides,[4] metal–organic coordination polymers,[5] and graphite carbon nitride (g-C_3N_4),[6–8] have been widely investigated for photocatalytic production of H_2O_2. Among them, g-C_3N_4 has drawn special attention as promising candidate due to high chemical stability, desirable visible light response, appropriate band structure, and ease of manufacture,[9–11] since the pioneering work by Shiraishi et al. [7] reported the photocatalytic activity toward H_2O_2 production over g-C_3N_4 under visible light illumination. The selective H_2O_2 production was considered to be due to the formation of 1,4-endoperoxide species on the surface of g-C_3N_4, which efficiently suppress the one-electron reduction of O_2 to form ·OOH radicals and is readily transformed to H_2O_2. Nevertheless, the photocatalytic performance of pristine g-C_3N_4 is still severely restricted by the intrinsic limitations such as small specific surface area, poor light absorption ability, high recombination rate of photo-generated electrons and holes, and low chemical adsorption capability of O_2 on its surface. In this regard, considerable efforts have been made to enhance the photocatalytic performance of g-C_3N_4-based materials toward H_2O_2 production from the respects of specific surface area, electronic and optical properties of g-C_3N_4. Correspondingly, various strategies have been put forwarded to optimize the aforementioned properties, including morphological control,[12] heteroatoms doping,[13,14] defect engineering,[15,16] chemical structural modification with organic molecules,[17,18] and hybridization with metal co-catalysts.[19] Especially, the introduction of nitrogen vacancies into the g-C_3N_4 framework was considered as an efficient strategy to not only modify the electronic structure for enhancing the light absorption, and also act as specific reactive sites for catalytic reactions,[20] thus significantly improving the photocatalytic activity of g-C_3N_4. To date, the reported strategies for the introduction nitrogen vacancies mainly took one of two approaches: (1) direct pyrolysis of argon atmosphere[21]; (2) post-treatment in the presence of reluctant agents ($NaBH_4$ and N_2H_4) or H_2 plasma.[22–24] Although great progress has been made, there is much room for improvement in the following respects: (1) the H_2O_2 yield still remains low and need be further improved prior to practical commercialization applications; (2) it remains unclear for some important fundamental aspects, especially about the understanding of the catalytically active sites for the H_2O_2 production, partly because of the inevitable co-existence of chemically distinct nitrogen vacancies the polymeric carbon nitride framework and the lack of their direct experimental observations. This report attempts to change that.

In the present work, we reported the synthesis of g-C_3N_4 materials possessing different nitrogen vacancies types by direct pyrolysis of melamine precursor under argon and ammonia atmosphere with the subsequent nitric acid oxidation, respectively. The pyrolysis atmosphere was found to have a significant influence on the introduced nitrogen vacancies type, specific surface area, band structure, and oxygen absorption ability of the resultant g-C_3N_4 materials, which contributed to the enhanced photocatalytic performance of the optimal catalyst toward H_2O_2 production.

2 | RESULTS AND DISCUSSION

The crystal structures of all the resultant catalysts were characterized by means of powder X-ray diffraction (XRD). As observed, there were two characteristic diffraction peaks of g-C_3N_4 at around 13.1° and 27.6° for all the resultant catalysts (Figures 1A and S1A), corresponding to be the (100) plane of the in-plane structural packing and the (002) plane of interlayer stacking of the tri-s-triazine rings, respectively.[25] This result indicated that different heat treatments did not affect the basic structural motif of g-C_3N_4. However, it can be noticed that the diffraction angles of the (002) peak for the resultant NH_3−CN and NH_3−O−CN were slightly shifted toward a higher value than those of Ar−CN and Ar−O−CN, suggesting the decrease in the interlayer stacking distance after ammonia pyrolysis. This phenomenon may be due to the replacement of carbon atoms by foreign nitrogen atoms in the framework of g-C_3N_4, leading to the lattice distortion of the graphitic structure.[26]

Fourier transform infrared (FTIR) spectroscopy was performed to further investigate the chemical structures of the resultant catalysts (Figures 1B and S1B). All the resultant

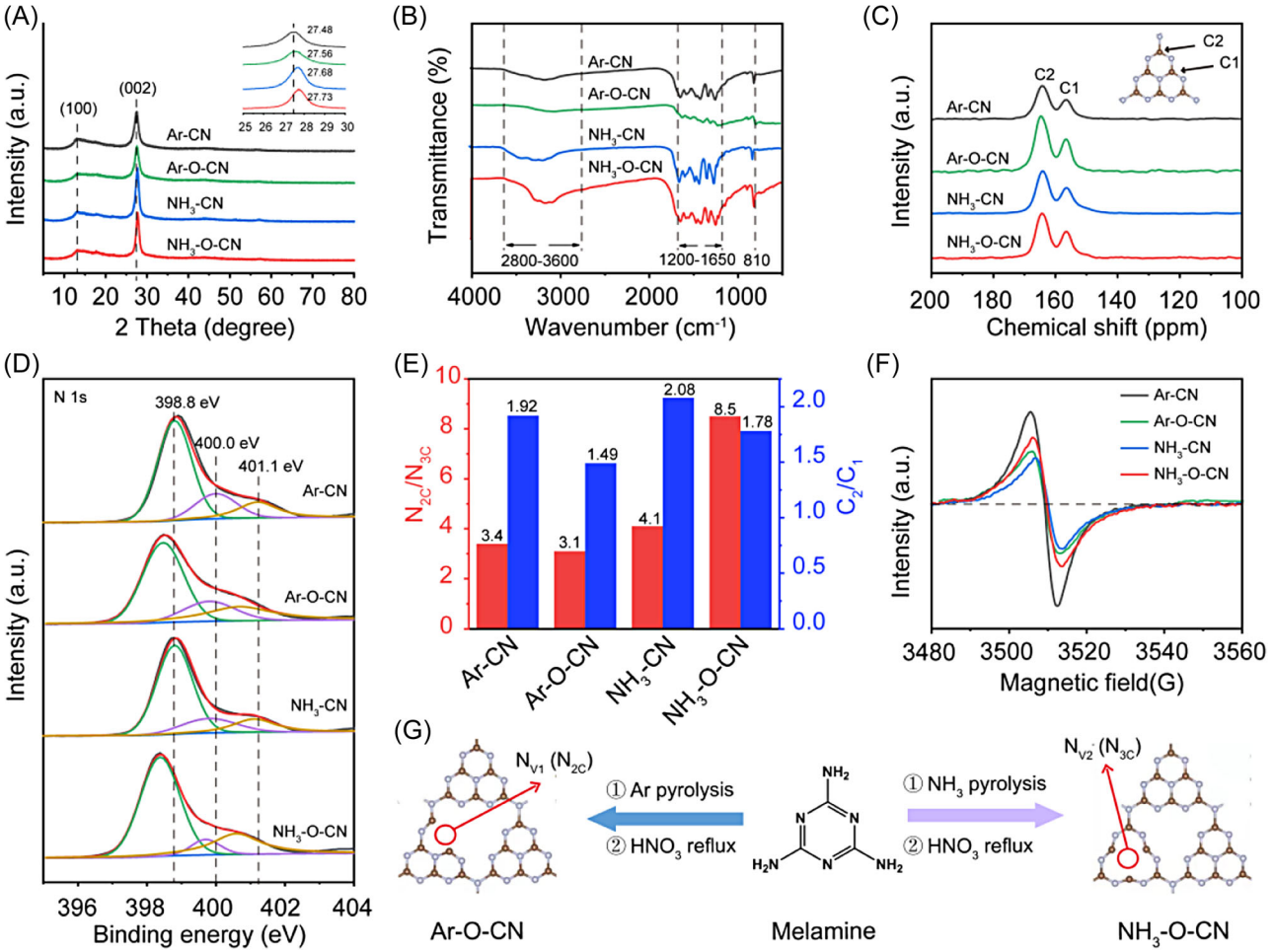

FIGURE 1 (A) X-ray diffraction (XRD) patterns, (B) Fourier transform infrared (FTIR) spectra, (C) solid-state nuclear magnetic resonances (NMR) spectra ^{13}C, and (D) high-resolution X-ray photoelectron spectroscopy (XPS) spectra of N 1s of the resultant Ar–CN, NH_3–CN, Ar–O–CN, and NH_3–O–CN; (E) N_{2C}/N_{3C} and C2/C1 value from (C) and (D); (F) electron paramagnetic resonance (EPR) spectra of the resultant Ar–CN, NH_3–CN, Ar–O–CN, and NH_3–O–CN; (G) schematic diagram of catalyst preparation process.

catalysts exhibited a sharp absorption peak at 810 cm^{-1} and a broad absorption peak in the both range of 1200–1650 cm^{-1} assigned to the characteristic out-of-plane bending and stretching vibration modes of the tri-s-triazine rings, respectively, revealing the formation of the graphitic carbon nitride structure.[13] Moreover, no obvious change in the characteristic bands between 1200 and 1650 cm^{-1} for all the resultant catalysts indicated that the skeleton of original g-C_3N_4 remains almost unchanged, which is consistent with the XRD results. Besides, there was another broad absorption peak at 2800–3600 cm^{-1}, which could be ascribed to the characteristic stretching vibration modes of N−H or O−H bonds from the surface uncondensed amine groups or the absorbed H_2O.[13] Close observations demonstrated the increase of the intensity of the peak in the range of 2800 and 3600 cm^{-1} whereas the decrease at around 810 cm^{-1} for the resultant NH_3−CN compared to Ar−CN, reflecting the introduction of more amino groups and the change of the tri-s-triazine rings. In the contrast, the resultant NH_3−O−CN exhibited the decreased intensity at 2800–3600 cm^{-1} after HNO_3 oxidation treatment, probably due to the oxidation of the amino groups.

Solid-state ^{13}C magic angle spinning nuclear magnetic resonances spectroscopy was also performed to get the insight about the specific structure information of the resultant catalysts with different heat treatments. There are two characteristic peaks at about 164.2 and 156.4 ppm for all the resultant catalysts (Figure 1C), which can be attributed to the C1 atoms and the C2 atoms in g-C_3N_4 skeleton.[27] Moreover, the decreased area ratio of C2 and C1 over the resultant Ar−O−CN and NH_3−O−CN was observed compared to Ar−O−CN and NH_3−O−CN (Figure 1E), indicating the formation of N vacancies induced by the HNO_3 oxidation treatment.

The surface element compositions and chemical states as well as defects information within the resultant catalysts were further unveiled by X-ray photoelectron spectroscopy (XPS). The survey spectra indicate the presence of C,

N, and O within all the catalysts (Figures S1C and S2A and Table S1). Careful observation clearly demonstrates the presence of the relatively higher content of oxygen within the resultant Ar–O–CN and NH_3–O–CN compared to other catalysts without the oxidation treatment of HNO_3, which may be due to the introduction of oxygen-containing functional groups. Moreover, the increased ratio of C to N was also observed after the oxidation treatment of HNO_3, indicating the formation of nitrogen vacancies. From the high-resolution XPS spectra of C 1s (Figures S1D and S2B), three deconvoluted peaks could be observed for the resultant Ar–CN, Ar–O–CN, NH_3–CN, and NH_3–O–CN at the binding energy of around 287.9 and 284.6 eV, corresponding to the sp^2-hybridized tertiary carbon in N-containing aromatic skeleton rings (N–C=N) and the adventitious type carbon (C–C), respectively.[13] It can be noticed that the peak area ratios of N–C=N to C–C were calculated to be 8.71 and 12.0 for Ar–CN and NH_3–CN (Table S2), respectively. The decrease of the tertiary carbon content percentage further confirmed the formation of nitrogen vacancies, which could affect the reactivity of the catalysts for the photosynthesis of H_2O_2. Moreover, the further decrease in the corresponding peak area ratios for Ar–O–CN and NH_3–O–CN were also observed compared to Ar–CN and NH_3–CN, implying more formation of nitrogen vacancies after HNO_3 oxidation treatment. Besides, the high-resolution XPS spectra of N 1s (Figures 1D and S1E) could be fitted into three nitrogen species with the binding energy of 398.4, 399.7, and 400.7 eV, which were assigned to sp^2-hybridized nitrogen in C-containing tri-s-triazine rings (C–N=C, N_{2C}), the tertiary nitrogen groups attached to the tertiary carbon at the center and peripheral of the heptazine units (N–$(C)_3$, N_{3C}), and the surface amino functional groups (C–NH_x), respectively.[13] Careful observation demonstrated the decreased trend in the ratio of N_{2C} to N_{3C} from 3.4 in Ar–CN to 3.1 in Ar–O–CN (Figure 1E and Table S3), indicating that N_{2C} were the preferred sites for the formation of nitrogen vacancies after HNO_3 oxidation treatment of the resultant Ar–CN catalyst.[21] In the contrast, there was the increased trend in the ratio of N_{2C} to N_{3C} from 4.1 in NH_3–CN to 8.5 in NH_3–O–CN, indicating that N_{3C} were the preferred sites for the formation of nitrogen vacancies after HNO_3 oxidation treatment of the resultant NH_3–CN catalyst. It is worth mentioning that the negative shift of the main peak of N 1s spectra for the resultant Ar–O–CN and NH_3–O–CN catalysts may be due to the oxygen doping after the oxidation treatment of HNO_3, which would leave extra electrons and then are rearranged to contiguous C and N atoms through the delocalized p-conjugated networks.[28] Meanwhile, the high-resolution XPS spectra of O 1s could be deconvoluted into two peaks at 531.9 and 533.7 eV (Figures S1F and S2C), which were attributed to be C–O species and the absorbed H_2O.[13] Moreover, the increase in the peak area at 531.6 eV the resultant Ar–O–CN and NH_3–O–CN also suggested the formation of C–O species after HNO_3 oxidation treatment (Table S4), which probably act as catalytic active sites for oxygen reduction reaction (ORR).[29]

In order to further verify the formation of nitrogen vacancies, room-temperature electron paramagnetic resonance (EPR) spectra were conducted over the resultant catalysts under dark condition. The EPR spectra of the resultant catalysts displayed one single Lorentzian line at about 3510 G with a g value of 2.003 (Figure 1F), arising from the localized unpaired electrons of the sp^2-hybridized carbon atoms in the aromatic rings within π-bonded nano-sized clusters.[22] Compared with the resultant NH_3–CN, the stronger signal intensity of the resultant NH_3–O–CN hinted the promoted formation of unpaired electrons after the introduction of nitrogen vacancies,[23] which was consistent with the decrease of nitrogen content in the resultant NH_3–O–CN (Table S1). Compared with Ar–CN, the resultant NH_3–O–CN and NH_3–CN catalysts have decreased nitrogen vacancies probably due to the introduction of more N atoms during the preparation process under NH_3 atmosphere. Based on these results above, the type of the introduced nitrogen vacancies could be tuned by the pyrolysis atmosphere (Figure 1G).

The morphologic structures of the resultant catalysts were examined by means of field emission scanning electron microscopy (FESEM) and transmission electron microscopy (TEM). Here, the resultant NH_3–O–CN was firstly selected as the representative sample for the detailed characterizations. The resultant NH_3–O–CN exhibited two domains of small nanoparticles and irregular thick blocks with rough surface (Figure 2A), which was similar with that of the resultant NH_3–CN (Figure S3B). Careful observation demonstrated that the irregular thick blocks possessed the sandwich structure composed of layered shell and nanoparticle core. Differently, the irregular thick blocks with relatively smooth surface were observed for the resultant Ar–CN (Figure S3A). After nitric acid oxidation treatment, the surface of the resultant Ar–O–CN has been corroded and the irregular holey structures appeared (Figure S3C), which may arise from nitric acid oxidation etching. However, further ammonia heat treatment made the morphology of the resultant Ar–O–CN change into plate-like structure with no regular morphology (Figure S3D). TEM images revealed the similar aggregated sheet-like structures for the resultant NH_3–O–CN and NH_3–CN whereas the resultant Ar–CN exhibited irregular thick blocks with non-uniform networks (Figures 2B and S4). The corresponding elemental mapping images showed the even distribution of C, N, and O in the resultant NH_3–O–CN, indicating the incorporation of oxygen into the carbon nitride framework.

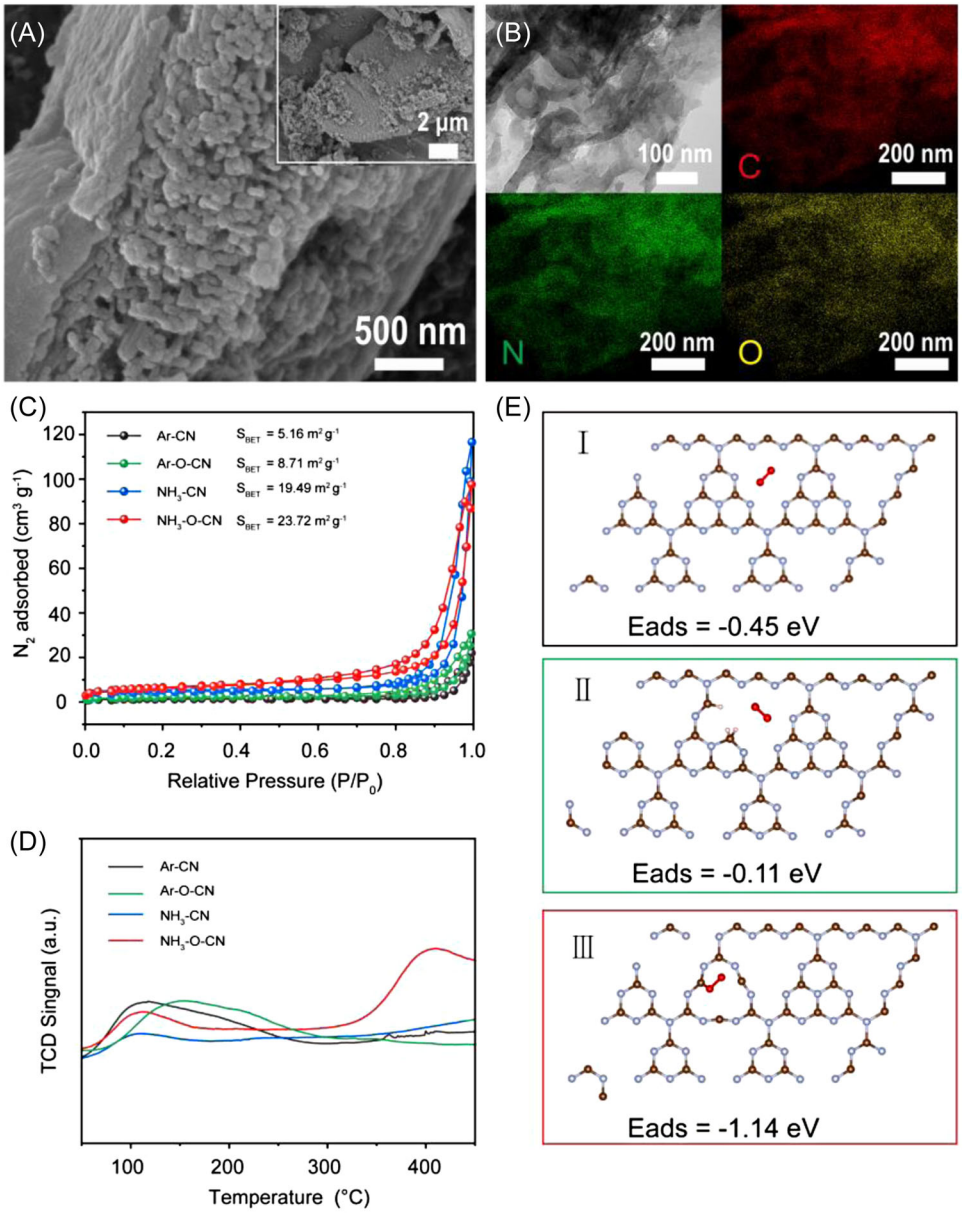

FIGURE 2 (A) Scanning electron microscopy (SEM) image and (B) transmission electron microscopy (TEM) image and the corresponding element mapping of the resultant NH_3–O–CN; (C) N_2 sorption isotherm and (D) oxygen temperature-programmed desorption (O_2-TPD) spectra of the resultant Ar–CN, Ar–O–CN, NH_3–CN, and NH_3–O–CN; (E) the top views of the optimal structure with O_2 molecule on different sites of CN with different nitrogen vacancies: (I) pristine CN without nitrogen vacancies, (II) CN with N_{v1}, and (III) CN with N_{v2}. Eads is the total adsorption energy of O_2.

The specific surface area has been widely considered be an important factor to determine the photocatalytic performance of the catalysts owing to the surface-dependent characteristic of the photocatalytic process.[15] The nitrogen sorption measurements were performed to determine the specific surface area of the resultant catalysts. All the resultant catalysts exhibited typical type IV isotherms according to the International Union of Pure and Applied Chemistry classification (Figures 2C and S5A), indicating the presence of mesopores. The calculated Brunauer–Emmett–Teller (BET) surface areas and Barret–Joyner–Halenda pore volumes of all the resultant catalysts were listed in Table S5. The BET surface areas exhibited the gradual increase in the order of Ar–CN (5.2 $m^2 g^{-1}$), Ar–O–CN (8.7 $m^2 g^{-1}$), NH_3–CN (19.5 $m^2 g^{-1}$), NH_3–O–CN (23.7 $m^2 g^{-1}$), and Ar–O–CN–NH_3 (123.6 $m^2 g^{-1}$), and similar increase trend of the pore volume for the resultant catalysts were observed. These indicated that ammonia heat treatment and HNO_3 oxidation treatment could significantly increase the BET surface areas of the resultant catalysts by optimizing the pore structure and surface properties. Meanwhile, the increased BET

surface area allowed for exposing more active sites and improving the adsorption capacity and accessibility of molecular oxygen to the active surface of the resultant catalysts,[15] thus facilitating the photocatalytic H_2O_2 production.

Since the adsorption of the reactants is an indispensable step for heterogeneous catalytic reactions, the oxygen temperature-programmed desorption (O_2-TPD) was performed to investigate the oxygen adsorption type and ability on the surface of the resultant catalysts (Figures 2D and S5B). There were two types of adsorbed oxygen species present on the resultant NH_3–O–CN compared to only one on the resultant NH_3–CN, Ar–CN, Ar–O–CN, and Ar–O–CN–NH_3, corresponding to the physisorption oxygen at around 100°C and the chemisorption oxygen at around 380°C, respectively.[15] This result demonstrated the strongest oxygen absorption ability over the resultant NH_3–O–CN, which was probably due to the introduction of nitrogen vacancies and the large surface area. Differently, the poor oxygen absorption ability over the resultant Ar–CN may arise from the less exposed oxygen adsorption sites on its surface due to the small surface area. In order to get a molecular-level insight into the influence of the nitrogen vacancies type on the oxygen absorption ability of g-C_3N_4, density functional theory (DFT) computations were performed. In addition to the conjugated melem constituted by the heptazine units as a model for the pristine g-C_3N_4, the models with different type of nitrogen vacancies were also established and the adsorption energy of oxygen at different sites was calculated (Figures 2E and S6). The calculated results demonstrated that the introduction of nitrogen vacancies generated from N_3C facilitates the enhancement in the oxygen absorption with highest oxygen absorption energy compared to the nitrogen vacancies (N_{v1}). Meanwhile, the improved oxygen absorption ability was reported to facilitate the formation of the 1,4-endoperoxide species in the case of g-C_3N_4 type materials,[13] which were key intermediates for the subsequent H_2O_2 production through two-electron oxygen reduction pathway. Therefore, it is reasonable to conclude that nitrogen vacancies as active sites could adsorb reactant oxygen molecules as well as trap the photo-generated electrons and promote the transfer of photo-generated electrons from the catalysts to the adsorbed oxygen molecules.

Light absorption capacity, the separation and recombination efficiency as well as transfer of the photo-generated electrons and holes over the catalysts have been widely considered to be important influencing factors on their photocatalytic performance. Thus, DFT computations were also performed to investigate the influence of the nitrogen vacancies type on the electronic band gap structure of g-C_3N_4 based on the established structural models with different type of nitrogen vacancies (Figure 3A–C). Unexpectedly, the introduction of nitrogen vacancies (N_{v2}) induced the red-shift in the absorption edge of the resultant NH_3–O–CN compared to the resultant Ar–CN, whereas there is a controversial result after the introduction of the nitrogen vacancies (N_{v1}). Further, ultraviolet−visible diffuse reflectance spectroscopy (UV−Vis DRS) spectra were utilized to investigate the optical absorption properties and the electronic band structure of the resultant catalysts. As shown, the resultant Ar–CN exhibited the characteristic absorption of graphitic carbon nitride with the absorption edge at approximately 450 nm (Figures 3D and S5C). As expected, the combination of ammonia heat treatment and the HNO_3 oxidation treatment also resulted in the enhanced light absorption for the resultant NH_3–O–CN, implying the more absorption of light energy and facilitating the improvement in the photocatalytic performance. In the contrast, a blue-shift in the absorption edge was observed after only ammonia heat treatment (NH_3–CN) or the HNO_3 oxidation treatment of the resultant Ar–CN (Ar–O–CN), which is in accordance with the DFT results. Furthermore, the band gap of the resultant catalysts can be generally obtained according to the Tauc equation (Equation 1)[24]:

$$\alpha h\nu = A\left(h\nu - E_g\right)^n \quad (1)$$

where α is the absorption coefficient, h is Planck constant, ν is photon frequency, E_g is band gap, and A is a constant. Considering the direct transition characteristic of graphitic carbon nitride, the value of n is 1/2. Therefore, the band gap can be derived from the tangent lines in the Tauc plot of $(\alpha h\nu)^{1/2}$ versus photon energy ($h\nu$), where the intercept of the tangent approximates the band gap of the resultant catalysts. The calculated band gaps of Ar–CN, Ar–O–CN, NH_3–CN, NH_3–O–CN, and Ar–O–CN–NH_3 were approximately 2.74, 2.76, 2.81, 2.62, and 2.74 eV (Figures 3E and S5D), respectively, indicating that ammonia heat treatment and HNO_3 oxidation treatment resulted in the narrowed band gap of the resultant NH_3–O–CN. Besides, valence band (VB) XPS was further conducted to determine the electronic structure and investigate the influence of different treatment methods on the relative positions of the conduction band (CB) minimum and VB maximum of the resultant catalysts. The VB maximum edge potentials of Ar–CN, Ar–O–CN, NH_3–CN, NH_3–O–CN, and Ar–O–CN–NH_3 were determined to be about 2.09, 2.19, 1.98, 2.04, and 2.02 V (Figures 3F and S5E), respectively. Careful observation demonstrated that ammonia heat treatment caused the negative shift of VB maximum position whereas HNO_3 oxidation treatment resulted in positive shift of VB maximum position. Combined with the UV–Vis DRS results, the corresponding CB minimum edge potentials

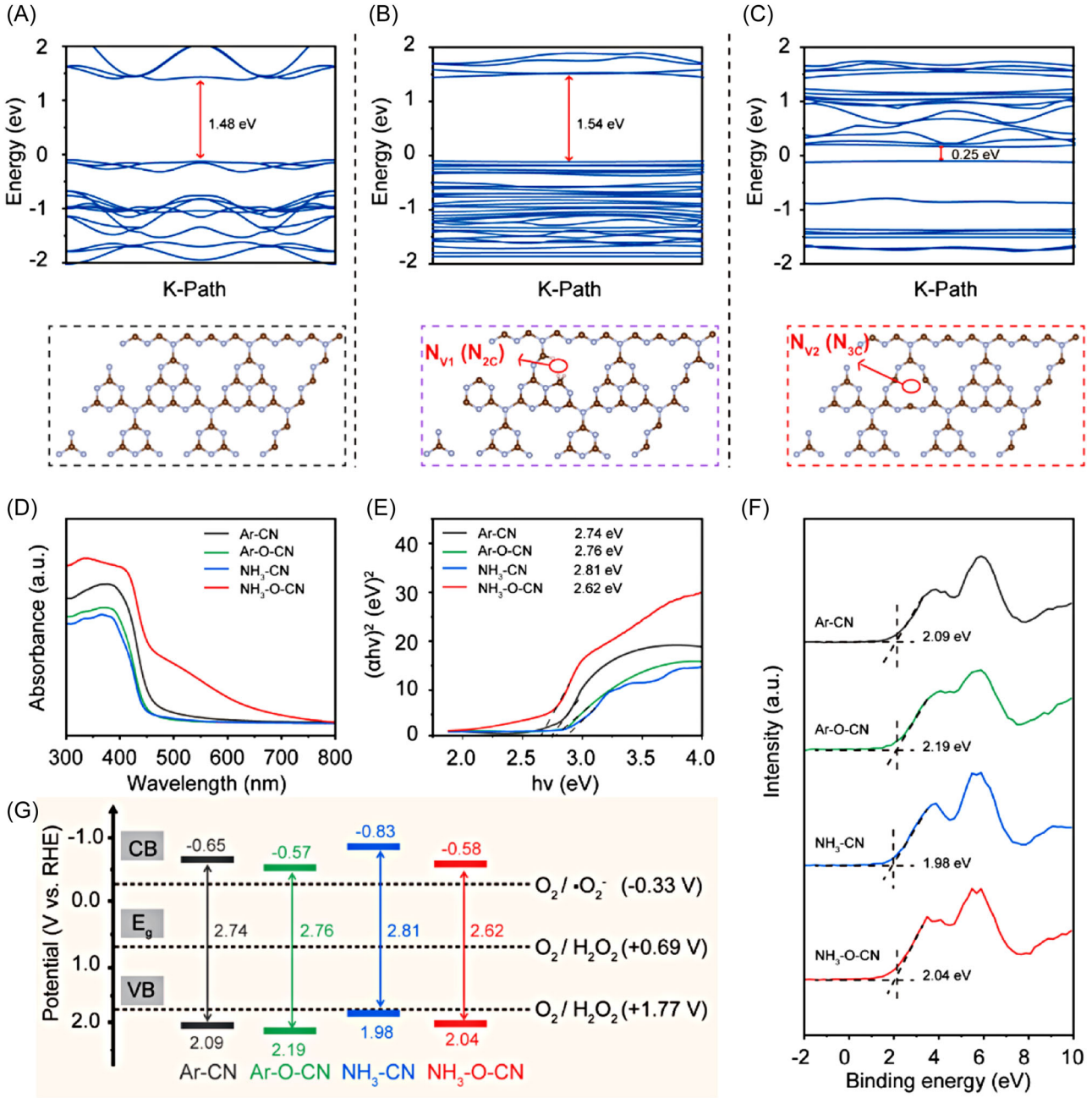

FIGURE 3 (A–C) The theoretically calculated band structure and structure model of Ar–CN (A), Ar–O–CN (N_{v1}, B), and NH_3–O–CN (N_{v2}, C); (D) UV–Vis diffuse reflectance spectra; (E) Tauc plots of $(\alpha h\nu)^2$ versus the energy of absorbed light; (F) valence band (VB) X-ray photoelectron spectroscopy (XPS) spectra; (G) the estimated band structure.

of these catalysts could be accordingly calculated to be -0.67, -0.57, -0.83, -0.58, and -0.72 V (Figures 3G and S5F), respectively, which were more negative than the redox potential of O_2/H_2O_2 (0.69 V). The large energy difference promoted well the reduction of O_2 to H_2O_2. Moreover, the narrowed band gap energy with the negative CB minimum edge potential could lead to the improvement in the redox ability of photo-generated electrons over the resultant catalysts, which was beneficial for the H_2O_2 production by the ORR process.

A photoluminescence (PL) technique was employed to explore the recombination and separation behavior of photo-generated electron–hole pairs in the resultant catalysts. As shown, there was the strong emission peak at around 462 nm for the resultant Ar–CN and Ar–O–CN (Figure S7), which originated from the direct electron-hole recombination of band transition. In addition, there was unexpectedly the significant higher intensity in the PL emission peak of the resultant Ar–O–CN, NH_3–CN, and NH_3–O–CN in comparison to that of Ar–CN, demonstrat-

ing the more recombination of photo-generated electrons and holes. Nevertheless, combined with the UV–Vis DRS results, the enhanced light absorption was observed for the resultant NH_3–O–CN, implying the more generation of electrons and holes over these catalysts.

Photocatalytic performance of the resultant catalysts was evaluated by monitoring the amount of the produced H_2O_2 under illumination. In order to demonstrate the influence of the pyrolysis temperature on the photocatalytic performance, we also prepared Ar–CN at different pyrolysis temperatures including 460°C, 520°C, and 580°C, which were noted as Ar–CN–460, Ar–CN, and Ar–CN–580, respectively. Figure S8A displayed the time profiles for H_2O_2 production over the resultant Ar–CN–460, Ar–CN, and Ar–CN–580 catalysts. Obviously, the concentration of the produced H_2O_2 over all these three catalysts increased almost linearly with the prolonging irradiation time. Meanwhile, the resultant Ar–CN produced the highest amount of H_2O_2 (119.0 μM), which was slightly higher than the resultant Ar–CN–460 (110.4 μM) and 1.7 times higher than the resultant Ar–CN–580 (71.4 μM). Therefore, in the subsequent experiments, 520°C was selected as the optimal pyrolysis temperature. The different pyrolysis atmospheres were also further optimized, and the corresponding results were presented in Figure S8B. The yield H_2O_2 was found to be strongly dependent on the pyrolysis atmosphere, and the highest H_2O_2 yield over the resultant NH_3–CN could reach 180.6 μM, which was 1.5 and 2.2 times higher than the resultant Ar–CN (119.0 μM) and Air–CN catalysts (80.7 μM), respectively. Interestingly, the photocatalytic H_2O_2 production ability can be largely improved by HNO_3 oxidation treatment (Figure 4A). The maximum H_2O_2 yield of 451.8 μM could be achieved over the resultant NH_3–O–CN, which was significantly higher than that of the resultant NH_3–CN (119.0 μM). Similar improvement phenomenon was also observed for the resultant Ar–CN and Ar–O–CN obtained after HNO_3 oxidation treatment. Unexpectedly, significantly decrease in the photocatalytic H_2O_2 production ability was observed after further ammonia pyrolysis of the resultant Ar–O–CN (Figure S9). It can be also observed that except for Ar–O–CN–NH_3 catalyst, the resultant NH_3–O–CN catalyst possesses a sandwich structure with relatively large specific surface area, which contributed the enhanced performance for photocatalytic H_2O_2 production. In contrast, the Ar–O–CN–NH_3 catalyst exhibits a poor performance for photocatalytic H_2O_2 production even though possessing a sheet-like structure with largest specific surface area. We infer that the unexpected phenomenon may be explained by the fact that the surface oxygen-containing functional groups on the surface of the resultant Ar–O–CN could react with NH_3 at high temperature, thus blocking the catalytically active sites for ORR and resulting in the decreased significantly performance. These results demonstrated the significant influence of the pyrolysis temperature and atmosphere, especially, the sequence of ammonia pyrolysis treatment and nitric acid oxidation treatment on the photocatalytic H_2O_2 production ability of the resultant catalysts. Moreover, careful observation demonstrated an anti-correlated response between PL emission peak intensity and H_2O_2 production. Thus, we inferred that despite the high recombination rate, there were still more photo-generated electrons and holes participating in the subsequent photocatalytic process in the presence of ethanol, which may explain well the higher photocatalytic activity of the resultant NH_3–O–CN in the production of H_2O_2 from molecular oxygen.

It has been reported that H_2O_2 could decompose into H_2O and O_2 on the surface of the photocatalyst by the photo-generated holes (Equation 2) and electrons (Equation 3) owing to the thermodynamic instability of H_2O_2.[13] The overall production of H_2O_2 is thus determined by the two competitive processes of the formation and decomposition of H_2O_2 during the photocatalytic process. From this perspective, it is of importance to understand the formation and decomposition behavior of H_2O_2 over the resultant catalysts. Generally, the formation rate of H_2O_2 was considered to follow zero-order kinetics due to the continuous purge of O_2 into the reaction system whereas the decomposition rate of H_2O_2 followed first-order kinetics.[30] The corresponding kinetic constant could be calculated by the established kinetic model (Equation 4):

$$H_2O_2 + 2h^+ = 2H^+ + O_2 \quad (2)$$

$$H_2O_2 + 2e^- + 2H^+ = H_2O + O_2 \quad (3)$$

$$[H_2O_2] = \frac{K_f}{K_d}\left(1 - e^{K_d t}\right) \quad (4)$$

where K_f and K_d are the rate constants for the production and decomposition of H_2O_2, respectively, and t is the reaction time. After fitting the origin data from Figure 4A according to Equation (4), the calculated K_f and K_d values were plotted in Figure 4F and summarized in Table S6. The K_f value on the optimal NH_3–O–CN catalyst (3.511 μmol L^{-1} min^{-1}) was 4.1 times higher than that on the resultant Ar–CN catalyst (0.848 μmol L^{-1} min^{-1}), and the K_d value on the former (6.1×10^{-3} min^{-1}) was only 1.2 times higher than that on the latter (5.0×10^{-3} min^{-1}). Nevertheless, the K_f value increased more than the K_d value, thus leading to the higher H_2O_2 yield after ammonia pyrolysis treatment and nitric acid oxidation treatment. Meanwhile, the H_2O_2 formation rate was observed to outperform the decomposition rate for all the resultant catalysts, which well explained why H_2O_2 could be continuously produced with the time prolonging.

The influence of the introduction of sacrificial agent on the photocatalytic performance of the resultant

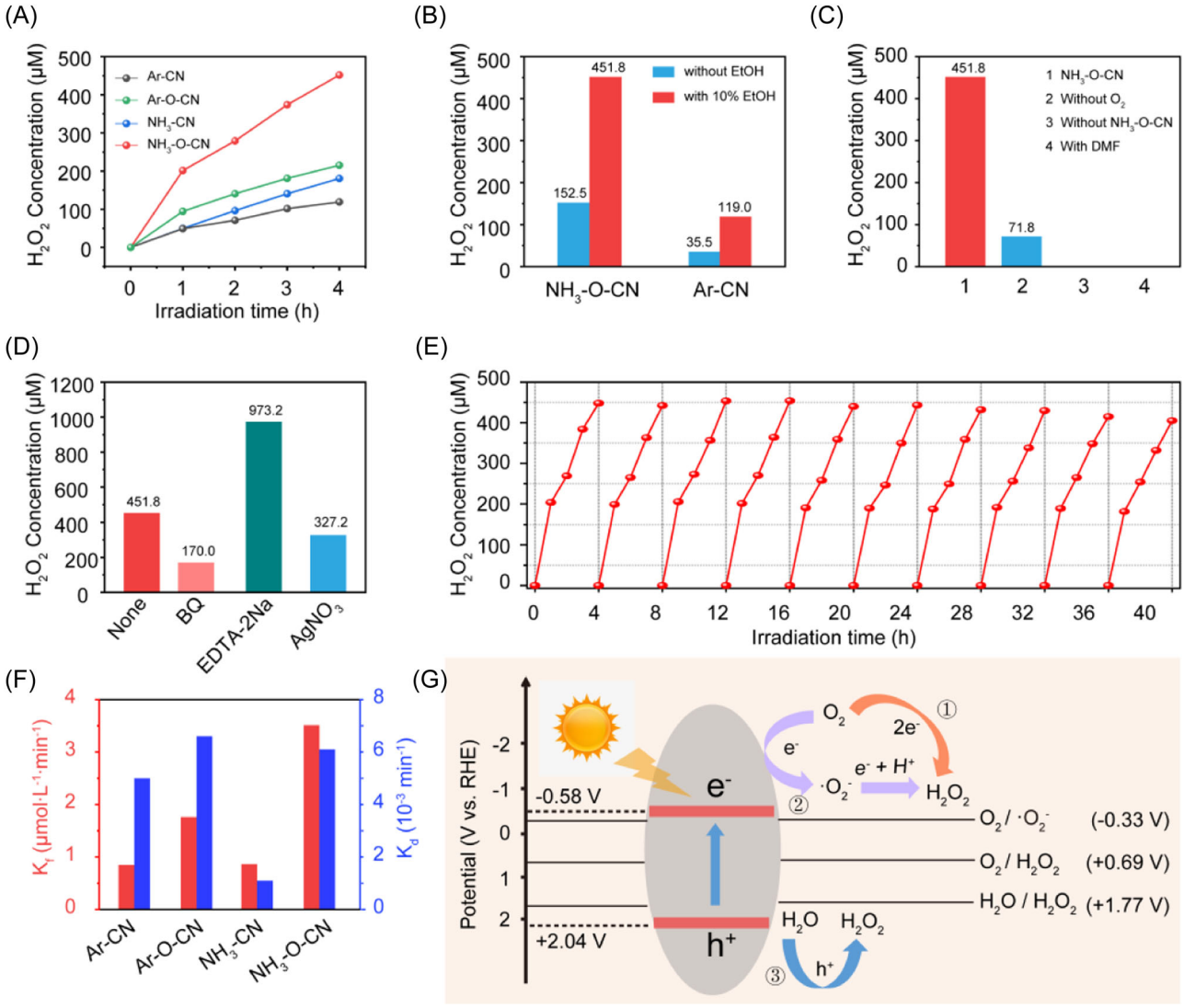

FIGURE 4 (A) The time profiles for H_2O_2 production over the resultant Ar–CN, Ar–O–CN, NH_3–CN, and NH_3–O–CN catalysts; (B) the amount of H_2O_2 produced over the resultant Ar–CN and NH_3–O–CN catalysts within 4 h in the presence and absence of ethanol (10% ethanol); (C) the amount of H_2O_2 produced over the resultant NH_3–O–CN catalyst within 4 h under different conditions: in the absence of O_2 (without O_2) and the resultant NH_3–O–CN catalyst, and in the presence of dimethylformamide (DMF) (with DMF); (D) the amount of H_2O_2 produced over the resultant NH_3–O–CN catalysts within 4 h after the addition of various scavengers including benzoquinone (BQ), ethylenediaminetetracetic acid disodium (EDTA-2Na), and $AgNO_3$; (E) cyclic stability test of the resultant NH_3–O–CN catalyst toward photocatalytic H_2O_2 production; (F) formation rate constant (K_f) and decomposition rate constant (K_d) for H_2O_2 production over the resultant Ar–CN, NH_3–CN, Ar–O–CN, and NH_3–O–CN. Conditions: 1 g L^{-1} catalyst, an O_2-saturated aqueous solution with 10 vol% ethanol (EtOH), and Xe lamp (intensity 30 mW cm^{-2}); (G) possible catalytic mechanism of the resultant NH_3–O–CN catalyst toward H_2O_2 production.

NH_3–O–CN catalyst was also studied. As shown in Figure 4B, the H_2O_2 yield could reach 451.8 μM after the introduction of 10% ethanol (EtOH), which was much higher than that in an ethanol-free system (152.5 μM). The improved H_2O_2 yield could be attributed to the relative lower oxidation potential of ethanol (0.216 V vs. reversible hydrogen electrode (RHE) when acetaldehyde as oxidation product) to water oxidation (1.23 V vs. RHE),[14] thus readily being oxidized by photo-generated holes and thus promoting the generation of proton. This is why ethanol was chosen as sacrificial agent for the subsequent H_2O_2 production test over the resultant NH_3–O–CN catalyst. Similar results were observed for the resultant Ar–CN catalyst. Careful comparison demonstrated the higher H_2O_2 yield (152.5 μM) over the resultant NH_3–O–CN catalyst even in the absence of ethanol than that over the resultant Ar–CN catalyst in the presence of ethanol (119.0 μM) and in the absence of ethanol (35.5 μM). The result indicated the improved oxidation ability of the photo-generated holes toward water oxidation during the photocatalytic process after ammonia pyrolysis and HNO_3 oxidation treatment. Further, H_2O_2 production cannot be observed

when dimethylformamide (aprotic solvent) instead of water was added into the reaction system (Figure 4C), revealing the necessity of H_2O as the proton source for H_2O_2 production.

In order to reveal the mechanism of photocatalytic H_2O_2 production over the resultant NH_3–O–CN catalyst, different reaction conditions were investigated (Figure 4C). It can be observed that there was an obvious decrease in H_2O_2 yield over the resultant NH_3–O–CN catalyst in the absence of O_2 compared to that in the presence of O_2, which only produced 71.8 μM H_2O_2. Meanwhile, no detectable amount of H_2O_2 was produced in the absence of the resultant NH_3–O–CN catalyst. These results confirmed that H_2O_2 production mainly originated from the photocatalytic O_2 reduction process. Nevertheless, a small amount of H_2O_2 production over the resultant NH_3–O–CN catalyst in the absence of O_2 also implied that H_2O_2 production may be caused from water oxidation in addition to O_2 reduction, which may be explained from the following aspects. Considering that the VB maximum edge potential (+2.04 V vs. RHE) of the resultant NH_3–O–CN catalyst was slightly positive relative to the redox potentials of $\cdot OH/OH^-$ (+1.99 V vs. RHE) whereas more positive than that of O_2/H_2O (+1.23 V vs. RHE) and H_2O_2/H_2O (+1.77 V vs. RHE), there were two possible reaction pathways for H_2O_2 production in the absence of O_2: (1) one-step: water was directly oxidized to H_2O_2; (2) two consecutive steps: water was first oxidized into O_2 by photo-generated holes, and then the produced O_2 was further reduced to produce H_2O_2 by photo-generated electrons. Besides, various active species trapping experiments were also carried out (Figure 4D). In detail, $AgNO_3$ (10 mmol L^{-1}), ethylenediaminetetracetic acid disodium (EDTA-2Na) (1 mmol L^{-1}), and 1,4-benzoquinone (BQ, 1 mmol L^{-1}) were introduced into the photocatalytic H_2O_2 production reaction system as the electron (e^-), hole (h^+), and superoxide radical ($\cdot O_2^-$) scavengers,[31] respectively. Unexpectedly, the H_2O_2 yield over the resultant NH_3–O–CN catalyst could still maintain 327.2 μM with insignificant decrease after the addition of $AgNO_3$, further revealing that H_2O_2 production was not only due to O_2 reduction. Combining with the result obtained in the absence of O_2 above, we inferred that water oxidation to H_2O_2 may be another dominant reaction pathway for H_2O_2 production in addition to O_2 reduction. Differently, the addition of EDTA-2Na induced the significant increase in the H_2O_2 yield up to 973.2 μM over the resultant NH_3–O–CN catalyst, which could be explained by the fact that EDTA-2Na could efficiently trap the photo-generated holes and thus make more photo-generated electrons participate in the process of O_2 reduction to produce H_2O_2 with minimizing the H_2O_2 decomposition. In the contrast, the addition of BQ greatly inhibited the H_2O_2 production down to 170.0 μM over the resultant NH_3–O–CN catalyst, indicating that $\cdot O_2^-$ may be an important intermediate for H_2O_2 production. Therefore, it could be speculated that H_2O_2 production over the resultant NH_3–O–CN catalyst may be partially achieved through a consequent two-step single-electron O_2 reduction process ($O_2 \rightarrow \cdot O_2^- \rightarrow H_2O_2$).

Since the cyclic stability of the catalysts was also one of the important parameters for their practical application, 10 runs of photocatalytic H_2O_2 production test over the resultant NH_3–O–CN catalyst were performed under the same conditions. In detail, the resultant NH_3–O–CN catalyst was separated by filtration and washed three times with deionized water after each photocatalytic run, and reused in a successive run. As observed, no significant change in the H_2O_2 yield was observed after 10 photocatalytic runs (Figure 4E), confirming its good cyclic stability. The marginal decrease in activity may be due to the catalyst loss during the repeated catalyst recovery process. XRD, XPS, and EPR were also performed to characterize the structural stability of the nitrogen vacancies for the on the cycled catalyst (Figure S10). As shown in Figure S10A,B, there is no change in the crystal structure and chemical composition for the cycled catalyst. Moreover, no obvious change in the ratio of C to N before and after cyclic test implies that nitrogen vacancies still exist in the catalyst structure, which is also verified by EPR result (Figure S10C,D). In a word, the excellent photocatalytic production ability of H_2O_2 with good cyclic stability of the resultant NH_3–O–CN catalyst made it promising in practical applications.

Based on the discussions above, the possible reaction mechanism for photocatalytic production of H_2O_2 was proposed and displayed in Figure 4G. Under illumination, electrons (e^-) and holes (h^+) are generated in the CB and VB of the photocatalyst, respectively. In the presence of water and ethanol, the photo-generated holes partially oxidized ethanol to acetaldehyde and partially oxidized water to H_2O_2 by two-electron pathway, whereas the photo-generated electrons reduced oxygen to H_2O_2 by two-electron pathway and $\cdot O_2^-$ by single-electron pathway, respectively. Moreover, the enhanced activity of the resultant NH_3–O–CN catalyst toward H_2O_2 production may be ascribed to the following respects: (1) enhancing light absorption in the whole UV–Vis region, especially in UV region; (2) increasing the specific surface area; (3) the strong oxygen absorption ability.

3 | CONCLUSION

In summary, we developed a facile method to fabricate g-C_3N_4 photocatalyst with different types of nitrogen vacancies by tuning the pyrolysis atmosphere. Ammonia pyrolysis was found to facilitate the introduction of

nitrogen vacancies (N_{v2}) from the tertiary nitrogen groups attached to the tertiary carbon (N_{3C}) where argon pyrolysis resulted in the formation of nitrogen vacancies (N_{v1}) from sp^2-hybridized nitrogen atoms in tri-s-triazine rings (N_{2C}). Moreover, the narrowed band gap and improved oxygen absorption ability were also observed due to the introduction nitrogen vacancies (N_{v2}), which contributed to the higher H_2O_2 yield of 451.8 μM over the resultant NH_3–O–CN catalyst than that of Ar–CN (119.0 μM), and good cyclic stability.

4 | EXPERIMENTAL

4.1 | Chemicals

Melamine ($C_3H_6N_6$, 99.0%), hydrogen peroxide (H_2O_2, 30%), and nitric acid (HNO_3, 65.0%–68.0%) were purchased from Sinopharm Chemical Reagent Co. Ltd. (China). Ethanol (C_2H_5OH, 99.7%) was purchased from Tianjin Fuyu Fine Chemical Co. Ltd. (China). All chemicals are used without further purification. Deionized water was obtained from laboratory water purification system (HHitech, Shanghai, China).

4.2 | Catalyst preparation

Typically, the polymeric CN was synthesized via direct pyrolysis of melamine in a tube furnace under NH_3 atmosphere at 520°C with the heating rate of 4°C min^{-1} for 4 h. After natural cooling to room temperature, the resultant product was collected and carefully ground into a powder, which was named as NH_3–CN. Subsequently, the resultant NH_3–CN was treated by refluxing with the mixture of concentrated HNO_3 and H_2O (v/v = 1:1, ca. 7.3 M) at 80°C for 3 h under magnetic stirring, and was then filtered and washed with ethanol and distilled water for several times, and dried at 60°C in a vacuum oven overnight, named as NH_3–O–CN. As comparison, we also prepared CN under Ar atmosphere and the corresponding treatment with HNO_3, which were named as Ar–CN and Ar–O–CN, respectively. Besides, the resultant Ar–O–CN was further treated under NH_3 atmosphere at 520°C for 4 h, named as Ar–O–CN–NH_3.

4.3 | Catalyst characterization

The morphologic structures of the resultant catalysts were characterized by FESEM (TESCAN, MIRA3 LMH) with an acceleration voltage of 5 kV and TEM with a Philips Tecnai G220 model microscope. The nitrogen sorption isotherms measurements were carried out in order to probe the pore and surface area of the resultant catalysts on an ASAP 2020-HD88 analyzer (Micromeritics Co. Ltd.). XRD patterns were recorded on a diffractometer (Bruker D8 Advance) using Cu K_α (λ = 1.5406 Å) radiation operating at 40 kV and 40 mA in the range from 5° to 90°. XPS and VB XPS were obtained on a spectrometer system with a monochromatic Al X-ray source (Thermo Scientific, K-Alpha). All binding energies were corrected based on the binding energy of C 1s peak at 284.8 eV to eliminate the charge effect. FTIR spectroscopy was measured on a spectrometer (NICOLET IS10) in the range from 4000 to 500 cm^{-1} with a resolution of 1 cm^{-1}. UV–Vis DRS were acquired by a UV–Vis spectrophotometer (PerkinElmer, Lambda 750) equipped with an integrating sphere attachment within the range of 200–800 nm and $BaSO_4$ as reference. The room-temperature PL spectra were measured on a FS5 fluorescence spectrophotometer (Edinburgh Instruments Ltd., Edinburgh, UK) using a Xenon lamp as excitation source at an excitation wavelength of 380 nm. The EPR spectra were recorded with a Bruker EMX plus EPR spectrometer at an X-band frequency of 9.84 GHz, sweep width of 1000.00 Gauss, and center field of 3450.00 Gauss. The O_2-TPD were measured by an Autochem II 2920 instrument (Micromeritics, USA). The detailed O_2-TPD measurement procedure is following: firstly, the catalysts were placed into a quartz U-tube reactor and were pretreated by temperature-programmed heat to 300°C with the heating rate of 10°C min^{-1} for 2 h in a flow of He gas (50 ml min^{-1}); secondly, after cooling down to 50°C, 10% O_2/He was purged for 0.5 h till stable baseline was obtained; thirdly, the O_2 desorption measurement was achieved by temperature-programmed heat to 500°C with the heating rate of 10°C min^{-1} under He atmosphere.

4.4 | First principles calculations

All calculations in this study were performed with the Vienna ab initio Simulation Package within the frame of DFT.[32] The exchange-correlation interactions of electron were described via the generalized gradient approximation with Perdew-Burke-Ernzerhof functional,[33] and the projector augmented wave method was used to describe the interactions of electron and ion.[34] The Monkhorst–Pack scheme with a 2 × 3 × 1 k-point mesh was used for the integration in the irreducible Brillouin zone.[35] The kinetic energy cut-off of 500 eV was chosen for the plane wave expansion. The lattice parameters and ionic position were fully relaxed, and the total energy was converged within 10^{-5} eV per formula unit. The final forces on all ions are less than 0.02 $Å^{-1}$. The corresponding band gap is calculated based on the set conditions above, and the adsorption

energies (Eads) were calculated according to the following equation: Eads = Ead/sub − Ead − Esub, where Ead/sub, Ead, and Esub are the total energies of the optimized adsorbate/substrate system, the adsorbate in the gas phase, and the clean substrate, respectively.

4.5 | Photocatalytic H_2O_2 production

The photocatalytic performance toward H_2O_2 production was evaluated by photo-irradiating O_2-saturated catalyst suspension containing the resultant catalysts and deionized water in the presence of ethanol as the electron and proton donor. Typically, the resultant suspension was firstly purged with oxygen for 20 min under continuous stirring prior to illumination, and then was irradiated by a Xenon lamp (Perfect Light, PLS-FX300HU) with the power density of 30 mW cm^{-2} in the wavelength range from 320 to 780 nm. At the given time intervals, 1 ml of solution sample was taken from the suspension and immediately centrifuged, and the concentration of the produced H_2O_2 was determined by a UV–Vis spectrophotometer (Shanghai Yoke Instrument Co. Ltd., T2600). In detail, 500 μl of supernatant liquid was reacted with 0.1 M KI (2 ml) and 0.01 M $H_{24}Mo_7N_6O_{24}{\cdot}4H_2O$ (50 μl), and then the absorbance of the solution was measured with a UV–Vis spectrometer at 352 nm after reaction for 5 min. Finally, the concentration of H_2O_2 can be calculated according to the prepared standard curves.

ACKNOWLEDGMENTS

This work is financially supported by Fundamental Research Funds for the Central Universities (Nos. 531118010232 and 202044011), Huxiang High-Level Talent Gathering Project of Hunan Province (No. 2019RS1012), and Natural Science Foundation of Changsha (No. KQ2202146).

CONFLICT OF INTEREST

The authors declare no conflicts of interest.

ORCID

Lei Han https://orcid.org/0000-0003-0186-2772

REFERENCES

1. Teng Z, Zhang Q, Yang H, et al. Atomically dispersed antimony on carbon nitride for the artificial photosynthesis of hydrogen peroxide. *Nat Catal*. 2021;4(5):374-384.
2. Sun Y, Han L, Strasser P. A comparative perspective of electrochemical and photochemical approaches for catalytic H_2O_2 production. *Chem Soc Rev*. 2020;49(18):6605-6631.
3. Sayama K. Production of high-value-added chemicals on oxide semiconductor photoanodes under visible light for solar chemical-conversion processes. *ACS Energy Lett*. 2018;3(5):1093-1101.
4. Hirakawa H, Shiota S, Shiraishi Y, Sakamoto H, Ichikawa S, Hirai T. Au nanoparticles supported on BiVO 4: effective inorganic photocatalysts for H_2O_2 production from water and O_2 under visible light. *ACS Catal*. 2016;6(8):4976-4982.
5. Zhuang H, Yang L, Xu J, et al. Robust photocatalytic H_2O_2 production by octahedral $Cd_3(C_3N_3S_3)_2$ coordination polymer under visible light. *Sci Rep*. 2015;5(1):16947.
6. Torres-Pinto A, Sampaio MJ, Silva CG, Faria JL, Silva AMT. Metal-free carbon nitride photocatalysis with in situ hydrogen peroxide generation for the degradation of aromatic compounds. *Appl Catal B: Environ*. 2019;252:128-137.
7. Shiraishi Y, Kanazawa S, Sugano Y, et al. Highly selective production of hydrogen peroxide on graphitic carbon nitride (g-C_3N_4) photocatalyst activated by visible light. *ACS Catal*. 2014;4(3):774-780.
8. Che H, Gao X, Chen J, Hou J, Ao Y, Wang P. Iodide-induced fragmentation of polymerized hydrophilic carbon nitride for high performance quasi-homogeneous photocatalytic H_2O_2 production. *Angew Chem Int Ed*. 2021;60(48):25546-25550.
9. Tian J, Wang D, Li S, et al. KOH-assisted band engineering of polymeric carbon nitride for visible light photocatalytic oxygen reduction to hydrogen peroxide. *ACS Sustain Chem Eng*. 2019;8(1):594-603.
10. Luo J, Fan C, Tang L, et al. Reveal Bønsted-Evans-Polanyi relation and attack mechanisms of reactive oxygen species for photocatalytic H_2O_2 production. *Appl Catal B: Environ*. 2022;301:120757.
11. Zhao Y, Zhang P, Yang Z, et al, Mechanistic analysis of multiple processes controlling solar-driven H_2O_2 synthesis using engineered polymeric carbon nitride *Nat Commun*. 2021;12(1):3701.
12. Lei J, Chen B, Lv W, et al. Robust photocatalytic H_2O_2 production over inverse opal g-C_3N_4 with carbon vacancy under visible light. *ACS Sustain Chem Eng*. 2019;7(19):16467-16473.
13. Samanta S, Yadav R, Kumar A, Kumar Sinha A, Srivastava R. Surface modified C, O co-doped polymeric g-C_3N_4 as an efficient photocatalyst for visible light assisted CO_2 reduction and H_2O_2 production. *Appl Catal B: Environ*. 2019;259:118054.
14. Moon G-h, Fujitsuka M, Kim S, Majima T, Wang X, Choi W. Eco-friendly photochemical production of H_2O_2 through O_2 reduction over carbon nitride frameworks incorporated with multiple heteroelements. *ACS Catal*. 2017;7(4):2886-2895.
15. Li S, Dong G, Hailili R, et al. Effective photocatalytic H_2O_2 production under visible light irradiation at g-C_3N_4 modulated by carbon vacancies. *Appl Catal B: Environ*. 2016;190:26-35.
16. Chen L, Chen C, Yang Z, Li S, Chu C, Chen B. Simultaneously tuning band structure and oxygen reduction pathway toward high-efficient photocatalytic hydrogen peroxide production using cyano-rich graphitic carbon nitride. *Adv Funct Mater*. 2021;31(46):2105731.
17. Shiraishi Y, Kanazawa S, Kofuji Y, et al. Sunlight-driven hydrogen peroxide production from water and molecular oxygen by metal-free photocatalysts. *Angew Chem Int Ed*. 2014;53(49):13454-13459.
18. Kofuji Y, Isobe Y, Shiraishi Y, et al. Carbon nitride-aromatic diimide-graphene nanohybrids: metal-free photocatalysts for solar-to-hydrogen peroxide energy conversion with 0.2% efficiency. *Chem Soc*. 2016;138(31):10019-10025.

19. Peng Y, Wang L, Liu Y, Chen H, Lei J, Zhang J. Visible-light-driven photocatalytic H_2O_2 production on g-C_3N_4 loaded with CoP as a noble metal free cocatalyst. *Eur J Inorg Chem*. 2017(40):4797-4802.
20. Niu P, Liu G, Cheng H-M. nitrogen vacancy-promoted photocatalytic activity of graphitic carbon nitride. *J Phys Chem C*. 2012;116(20):11013-11018.
21. Fattahimoghaddam H, Mahvelati-Shamsabadi T, Lee B-K. Enhancement in photocatalytic H_2O_2 production over g-C_3N_4 nanostructures: a collaborative approach of nitrogen deficiency and supramolecular precursors. *ACS Sustain Chem Eng*. 2021;9(12):4520-4530.
22. Shi L, Yang L, Zhou W, et al. Photoassisted construction of holey defective g-C_3N_4 photocatalysts for efficient visible-light-driven H_2O_2 production. *Small*. 2018;14(9):1703142.
23. Qu X, Hu S, Li P, et al. The effect of embedding N vacancies into g-C_3N_4 on the photocatalytic H_2O_2 production ability via H_2 plasma treatment. *Diam Relat Mater*. 2018;86:159-166.
24. Zhu Z, Pan H, Murugananthan M, Gong J, Zhang Y. Visible light-driven photocatalytically active g-C_3N_4 material for enhanced generation of H_2O_2. *Appl Catal B: Environ*. 2018;232:19-25.
25. Kim S, Moon G-h, Kim H, et al. Selective charge transfer to dioxygen on KPF6-modified carbon nitride for photocatalytic synthesis of H_2O_2 under visible light. *J Catal*. 2018;357:51-58.
26. Wang H, Guan Y, Hu S, Pei Y, Ma W, Fan Z. Hydrothermal synthesis of band gap-tunable oxygen-doped g-C_3N_4 with outstanding-two-channel-photocatalytic H_2O_2 production ability assisted by dissolution-precipitation process. *Nano*. 2019;14(02):1950023.
27. Zhao C, Shi C, Li Q, et al. Nitrogen vacancy-rich porous carbon nitride nanosheets for efficient photocatalytic H_2O_2 production. *Mater Today Energy*. 2022;24:100926.
28. Zhang J, Hu Y, Li H, et al. Molecular self-assembly of oxygen deep-doped ultrathin C_3N_4 with a built-in electric field for efficient photocatalytic H_2 evolution. *Inorg Chem*. 2021;60:15782-15796.
29. Lu Z, Chen G, Siahrostami S, et al. High-efficiency oxygen reduction to hydrogen peroxide catalysed by oxidized carbon materials. *Nat Catal*. 2018;1(2):156-162.
30. Wang R, Zhang X, Li F, et al. Energy-level dependent H_2O_2 production on metal-free, carbon-content tunable carbon nitride photocatalysts. *J Energy Chem*. 2018;27(2):343-350.
31. Wang H, Fang L, Hu S, Pei Y, Ma W. A green and facile method to prepare graphitic carbon nitride nanosheets with outstanding photocatalytic H_2O_2 production ability via NaClO hydrothermal treatment. *New J Chem*. 2018;42(22):18335-18341.
32. Kresse G, Furthmuller J. Efficient iterative schemes for ab initio total-energy calculations using a plane-wave basis set. *Phys Rev B*. 1996;54(16):11169-11186.
33. Perdew JP, Burke K, Ernzerhof M. Generalized gradient approximation made simple. *Phys Rev Lett*. 1996;77(18):3865-3868.
34. Kresse G, Joubert J. From ultrasoft pseudopotentials to the projector augmented-wave method. *Phys Rev B*. 1999;59(3):1758-1775.
35. Monkhorst HJ, Pack JD. Special points for Brillouin-zone integrations. *Phys Rev B*. 1976;13(12):5188-5192.

SUPPORTING INFORMATION

Additional supporting information can be found online in the Supporting Information section at the end of this article.

How to cite this article: Zhu Y, Liu X, Liu H, et al. Regulating nitrogen vacancies within graphitic carbon nitride to boost photocatalytic hydrogen peroxide production. *SusMat*. 2022;2:617–629. https://doi.org/10.1002/sus2.83